Constraints on Earth-Moon dynamical parameters from Eocene cyclostratigraphy

Slah Boulila, Linda A. Hinnov

Published in Global and Planetary Change, vol. 216, 103925.
Available online 17 August 2022
https://doi.org/10.1016/j.gloplacha.2022.103925.

Constraints on Earth-Moon dynamical parameters from Eocene cyclostratigraphy

Slah Boulila [a,b,*], and Linda Hinnov [c]

[a] *Sorbonne Université, CNRS, Institut des Sciences de la Terre Paris, ISTeP, F-75005 Paris, France.*
[b] *ASD/IMCCE, CNRS-UMR8028, Observatoire de Paris, PSL University, Sorbonne Université, 77 Avenue Denfert-Rochereau, 75014 Paris, France.*
[c] *Department of Atmospheric, Oceanic, and Earth Sciences, George Mason University, Fairfax, VA 22030, USA.*

* *Corresponding author: slah.boulila@sorbonne-universite.fr*

Abstract

The theoretical prediction of Earth-Moon dynamics in deep geologic time is hampered by limited knowledge of Earth's past tidal dissipation and dynamical ellipticity. Cyclostratigraphy can, however, provide valuable information on the geologic evolution of the Earth-Moon dynamical parameters. Here we investigate Eocene cyclostratigraphy to estimate Earth's precession rate (*p*), Earth-Moon distance (EMD) and length-of-day (LOD). Two highly-resolved deep sea records are selected from the Atlantic Ocean, with ages centered on 42.5 Ma (40.9–44.3 Ma; IODP Site U1410) and 54.95 Ma (54.1–55.8 Ma; ODP Site 1262). The sedimentary sequences at these sites recorded Milankovitch forcing signals with prominent precession index (Site 1262) and obliquity (Site U1410) frequencies and their amplitude modulations. At Site U1410, amplitude modulation of the main obliquity cycle was tuned to the Earth's 173-kyr orbital inclination (s_3-s_6) metronome, and at Site 1262, the dominant precession index amplitude modulation to the 405-kyr orbital eccentricity (g_2-g_5) metronome. This enabled estimation of Earth's precession rate *p* of 51.486 ±0.064 arcsec/yr and 51.546 ±0.168 arcsec/yr for 42.5 Ma and 54.95 Ma, respectively. These *p* estimates indicate EMD values of 383.710 ± 0.090 x 10^3 km and 382.625 ±0.265 x10^3 km, and LOD values of 23.679 ± 0.0115 hours and 23.667 ±0.039 hours for 42.5 Ma and 54.95 Ma, respectively. These

estimates deviate from theoretical predictions based on back calculation assuming present-day tidal dissipation. In particular, a significant discrepancy between the model and observations (cyclostratigraphy) occurs at 54.95 Ma (Site 1262) suggesting contributions from other effects on Earth's rotation, including changes in tidal dissipation and/or Earth's dynamical ellipticity related to mantle convection and the early Eocene global warming.

Key words: Earth's axial precession, Earth-Moon distance, length-of-day, Eocene, ocean drilling.

1. Introduction

The Earth-Moon system has experienced significant rotational-orbital dynamics through time (Lambeck, 1980). Tidal dissipation operates continuously on the Earth-Moon system to cause deceleration of Earth rotation and acceleration of the Moon in its orbit as it recedes from the Earth to conserve angular momentum. Perturbations in the Earth's moments of inertia, or dynamical ellipticity, impose other, smaller fluctuations in Earth rotation rate, in addition to changes in flattening linked to the tidally influenced rotation rate. As a result, tidal dissipation and dynamical ellipticity affect Earth-Moon distance (EMD), Earth's rotation rate and length-of-day (LOD), and consequently Earth's precession rate (p).

Today, EMD and lunar recession rate are precisely measured using lunar laser ranging (LLR) to reflectors installed on the Moon nearly fifty years ago by the Apollo and Lunokhod missions. The present-day increase rate of lunar semi-major axis is 3.808 ± 0.019 cm/year (Williams et al., 2014) and present-day EMD (in terms of semi-major axis of the lunar orbit) is 384402 km (Murphy, 2013). LOD is precisely measured using very long baseline interferometry and other methods (McCarthy and Seidelmann, 2018); present-day LOD of 23.9345 hours (86164 sidereal seconds) is defined by the present-day Earth mean angular velocity of $\phi_0 = 7.2921150(1) \times 10^{-5}$ rad/s at J2000 (**Supplementary Material**).

EMD and LOD remain poorly known for most of the geological past. A small number of Paleozoic and Precambrian geological data supports a significantly shorter LOD in the past with respect to present day. Paleozoic fossils recording daily-seasonal and/or tidal variations have been long targeted by scientists (e.g., Rosenberg and Runcorn, 1975; Brosche and Sündermann, 1978). A handful of Precambrian and Paleozoic tidalites have also provided high-resolution data on ocean tides, affording independent information on LOD, lunar months per year and Earth-Moon distance (e.g., Runcorn, 1979; Lambeck, 1980; Deubner, 1990; Archer, 1996; Williams, 2000; Coughenour et al., 2009; Kvale, 2012).

By contrast, cyclostratigraphy offers the potential to provide bundled, quantitative estimates for p, LOD and EMD from the geological record of Milankovitch cycles throughout geologic time (Walker and Zahnle, 1986; Berger et al., 1989; Berger et al., 1992). Owing to their dependence on the Earth's precession rate (p), Milankovitch cycles can provide rich benchmarks for Earth-Moon dynamical parameters, to reconstruct a continuous history of the Earth-Moon system.

Predictions suggest that changes in Milankovitch cycle frequencies are not easily discerned after early Mesozoic-late Paleozoic time (i.e., post 250 Ma). This has motivated geologists to search for predicted shorter-period Milankovitch cycles primarily in Paleozoic and Precambrian cyclostratigraphy (e.g., Wu et al., 2013, 2019; Meyers and Malinverno, 2018). Consequently, there have been relatively few reports on Earth-Moon dynamics from Mesozoic cyclostratigraphy (Boulila et al., 2014; Li et al., 2016, 2018; Liu et al., 2020), or Cenozoic cyclostratigraphy (Pälike and Shackleton, 2000; Lourens et al., 2001; Zeeden et al., 2014; Meyers and Malinverno, 2018).

Eocene cyclostratigraphy from ocean drilling sites has recorded high-resolution precession index and obliquity forced paleoclimate cycles (e.g., Westerhold et al., 2007; Boulila et al., 2018). Here we analyze two intervals of Eocene cyclostratigraphy from 40.9 Ma to 55.8 Ma for Earth-Moon dynamical parameters, and compare them with model predictions. By Eocene time, the cumulative effects of tidal dissipation (if the present-day value is valid from Eocene to present) should be detectable in cyclostratigraphy. The principal objective of this study is to measure specific precession index and obliquity line frequencies, and from these frequencies estimate p, EMD and LOD. We compare these empirically estimated parameters to those of the La2004 precession model (Laskar et al., 2004) (**Table 1**) and to other empirical estimates for the early Eocene obtained by independent methods (Meyers and Malinverno, 2018; Zeebe and Lourens, 2022).

2. Data and methods

2.1. A north-south transect of Atlantic Ocean sediment drill sites

Early Cenozoic paleoclimate experienced global warming punctuated by several successive major warming events (**Fig. 1**) (Zachos et al., 2001; Westerhold et al., 2020). From this global warming time interval, two exceptional records have been collected by ocean drilling programs, ODP Site 1262 leading out of the Paleocene-Eocene Thermal Maximum (PETM, Zachos et al., 2005), and IODP Site U1410 into the Middle Eocene Climatic Optimum (MECO, Bohaty and

Zachos, 2003). The high quality of these records offers the best chance for accurate detection of individual harmonic lines of the Early Cenozoic obliquity and precession index.

IODP Site U1410 documents a strong obliquity signal modulated by the 173 kyr (s_3–s_6) orbital inclination cycle, expressed in high-resolution (2 cm) X-ray-fluorescence (XRF) derived Ca/Fe ratio data (Boulila et al., 2018). The studied interval at IODP Site U1410 covers Chrons C18r *p.p.* through C20n *p.p.* of the middle Eocene (**Fig. 2**, 40.9–44.3 Ma, see also **Supplementary Material**).

ODP Site 1262 records a strong precession index signal modulated by the short (~100 kyr) and long (405 kyr) (g_2–g_5) orbital eccentricity cycles, expressed in high-resolution (2 cm) XRF derived Fe data (Westerhold et al., 2007). The studied interval at ODP Site 1262 covers C24r *p.p.* of the early Eocene (**Fig. 3**, 54.1–55.8 Ma).

2.2. Astronomical metronomes and tuning procedure

The metronomic potential of the g_2–g_5 (405-kyr) orbital eccentricity and s_3-s_6 orbital inclination cycles are used to tune the sedimentary records. The g_2-g_5 eccentricity metronome is consistent over 0-55 Ma for the La2004 and La2010a-d solutions (Fig. 4.7 in Laskar, 2020). The s_3-s_6 inclination metronome indicates disagreement of approximately 40 kyr from 45 Ma to 55 Ma, and further disagreement prior to 55 Ma, among the La2004, La2010d, La2011 and La421 solutions (Fig. 2D in Boulila et al., 2018).

The two studied sites were tuned to these metronomes during times of maximum solution consistency (for high accuracy and precision): s_3-s_6 for obliquity-dominated IODP Site U1410 (40.9–44.3 Ma), on the obliquity modulation envelope in the proxy series, and g_2-g_5 for orbital eccentricity-precession index-dominated ODP Site 1262 (54.1–55.8 Ma), directly on the 405-kyr cycle in the proxy series (details in **Supplementary Material**).

Bandpass filtering of g_2-g_5 and s_3-s_6 metronome cycles was performed using the Gaussian filter function in *Analyseries* (Paillard et al., 1996). The strong linearity between astronomy and cyclostratigraphy at Site 1262 (e.g., Meyers and Malinverno, 2018) allows us to perform a single tuning based on the 405 kyr g_2-g_5 orbital eccentricity metronome (**Supplementary Material**). The 405 kyr tuning successfully calibrates the short orbital eccentricity and precession index frequencies (**Figs. 5** and **S3**). At Site U1410, sedimentation rate variability at high frequencies in the obliquity band (Boulila et al., 2018) precludes a simple tuning to the 173 kyr s_3-s_6 metronome cycle. Tuning the 2.81 m mean wavelength (**Fig. S1A**) to a 173 kyr cycle allows the time calibration of a substantial part of the middle Eocene timescale, but does not succeed in aligning high-frequency cycles to predicted obliquity frequencies (Boulila et al.,

2018). Here we proceeded differently. First, we tuned the stratigraphic cycle interpreted as O1 to periods ranging progressively from 37 to 41 kyr with an increment of 0.1 kyr. We retained the optimal O1 target value (38.7 kyr) that yields an average period of 173 kyr for the presumed s_3–s_6 modulation cycle (double peaks in **Fig. S1A**, Boulila et al., 2018). Then, we retuned the bandpass-filtered 173 kyr band in the 38.7-kyr-calibrated log(Ca/Fe) time series to a simple 173-kyr cycle. This second, 173 kyr stable tuning aligns the obliquity frequencies to reasonable values for this Eocene time interval (**Figs. 4** and **S1**).

2.3 Time series analysis

Multi-taper method (MTM) spectral analysis (Thomson, 1982) with three 2π prolate tapers and data adaptive weighting was used to assess harmonic line (also known as amplitude, or first moment) and associated F-variance ratio (F-test) spectra. MATLAB scripts for these procedures are available online (see **Supplementary Material**).

Multi-taper method (MTM) harmonic analysis approaching the Rayleigh frequency resolution of $\Delta f = 1/T$ for a time series of duration T is provided by the $c_0\pi$ prolate multi-taper method (Thomson, 1982, 2009). This approach provides a line estimator $\mu(f)$ and a significance test: $\rho(f)$ is the ratio of variance at single frequency f to the residual variance in the band $[f - W, f + W]$, where $W = c_0\,\mathrm{T}$, with time-bandwidth product $c_0 = NW$ for a uniformly sampled time series of length N, an effective averaging bandwidth $B = 2W$ and $2K - 1$ prolate tapers are used (Park et al., 1987), where $K = 2c_0$. This ratio comprises the F-test of two variances, i.e., $\rho(f) = F(f)$, that has an F-distribution of 2 and $2K - 2$ degrees of freedom (dofs) (Eq. 13.10 in Thomson, 1982). When data adaptive weighting is used, as in this study, then dofs will be lower in regions of the spectrum with reduced power, but will not drop below 2 dofs. $F(f)$ is also adjusted (downward in regions of low power) by the data adaptive weighting. An $F(f)$ value indicating a cumulative F-distribution of 0.95 indicates evidence for a line at frequency f at the 95% significance level. Here, $F(f)$ is used to constrain frequency uncertainty (see **Section 2.4**). Selected Milankovitch (precession index and obliquity) line frequencies interpreted visually from the amplitude spectra of Sites U1410 and 1262 were used in the calculation of p (see **Section 2.5**). In this study, $c_0 = 2$.

2.4 Line frequency uncertainty

Uncertainty in the measured precession index and obliquity line frequencies is estimated from the Cramér-Rao bound, which determines the lower limit on accuracy of an estimated line

frequency f, given that neighboring lines are no closer than the averaging bandwidth $W = 2/T$ for 2π multitapered spectra, although empirical evidence suggests that $F(f)$ "works well down to the Rayleigh resolution" (p. 560, Thomson, 1990). This uncertainty is reported as standard deviation SD in terms of frequency f and period P, as $SD\{f\}$ and $SD\{P\}$ (Eqs. 26 and 28 in Thomson, 2009). Additional information concerning the frequency separation of individual Milankovitch lines is provided in the **Supplementary Material**.

2.5 Modeling *p*, *EMD* and *LOD*

Earth's precession frequency (or rate) can be expressed as (e.g., Na, 2013):

$$p = \frac{3G}{2\phi} H \left[\frac{m_M}{a_M^3} + \frac{m_S}{a_S^3}\right] cos\ \varepsilon \qquad \text{Eq. 1}$$

where G is the constant of gravitation; ϕ is the Earth rotation rate; ε is the obliquity (axial tilt) angle; m_M is the lunar mass; m_S is the solar mass; a_M is the Earth-Moon distance (EMD; semi-major lunar axis); a_S is the Earth-Sun distance; and $H = (C - A)/C$ is the dynamical ellipticity, where A is the Earth polar moment of inertia, C is the Earth equatorial moment of inertia, and $H = H(\phi)$. This model assumes circular orbits for the Earth and Moon, present day obliquity angle ε, and hydrostatic Earth flattening for H that is dependent on rotation rate ϕ. The specific values used for all variables are discussed in the **Supplementary Material.**

Models for the geologic evolution of p variously assume a constant lunar recession rate based on the present-day rate (Berger et al., 1992), a constant tidal dissipation rate through geologic time (Laskar et al., 2004), or a lunar recession rate constrained by an increasing tidal dissipation (Waltham, 2015). There is little evidence to support any of these models.

Calculation of p from cyclostratigraphic observations of Milankovitch lines is:

$$p \pm \sigma_p = C_1 a - b \qquad \text{Eq. 2}$$

where a is the cyclostratigraphic line frequency (in cycles/yr) with uncertainty σ_a (in cycles/yr), as determined by $SD\{f\}$; b is the modeled fundamental secular frequency (in arcsec/yr) with uncertainty σ_b (in arcsec/yr) (**Table 2**); C_1 = 1296000 arcsec = 360º x 60 min/º x 60 arcsec/min; and by error propagation, $\sigma_p = \sigma_{a,b} = \sqrt{C_1^2\sigma_a^2 + \sigma_b^2}$. Uncertainties in the fundamental secular frequencies are based on Solar System modeling (Laskar et al., 2004), and in the case of Site 1262, from Bayesian analysis of cyclostratigraphy (Meyers and Malinverno, 2018).

EMD and LOD and their uncertainties are identified by searching through p (Equation 1) using the MATLAB script *earthmoonkandT.m* (see **Supplementary Material**).

3. Results

3.1 IODP Site U1410 (40.9-44.3 Ma)

Harmonic analysis of North Atlantic Site U1410 (**Fig. 4**) indicates a strong obliquity response of log(Ca/Fe); the distorted ("clipped") sinusoids divert power into the 173-kyr difference tone (s_3-s_6) that was used to tune the time series. The principal obliquity lines are recognizable at slightly higher frequencies than the present-day theoretical obliquity lines (**Table 1**). The lines are surrounded by elevated amplitudes suggestive of noise and/or frequency variability in the lines due to uncorrected sedimentation rates not corrected by the inclination metronome. The two highest amplitude lines have periods at 39620 ±63 yr and 38506 ±83 yr and are interpreted as p+s_3 and p+s_4; these are associated with elevated $F(f)$ values, although neither matches up precisely at a local maximum at the same f as the peak amplitudes.

3.2 ODP Site 1262 (54.1–55.8 Ma)

Harmonic analysis of South Atlantic Site 1262 (**Fig. 5**) indicates a strong precession-eccentricity response of Fe concentration; the distorted precession-scale sinusoids divert power into the orbital eccentricity band, including g_2-g_5 that was used to tune the time series. The principal precession index lines are recognizable at slightly higher frequencies than the present-day theoretical precession index lines (**Table 1**). The lines are surrounded by elevated amplitudes suggestive of noise and/or frequency variability in the lines due to uncorrected sedimentation rates not corrected by the eccentricity metronome. The two highest amplitude lines have periods at 21877 ± 68 yr and 18871 ± 54 yr and are interpreted as p+g_2 and p+g_3; these are associated with local maxima in $F(f)$ at or near the same f as the peak amplitudes.

3.3. Eocene *p*, EMD and LOD

The Earth-Moon dynamical parameters estimated from these Eocene cyclostratigraphic data may be compared to the La2004 precession model provided by Equation 40 in Laskar et al. (2004) and the smoothly increasing tidal (**Fig. 6**). Sites U1410 and 1262 at 42.5 Ma and 54.95 Ma indicate respectively p = 51.486 ±0.064 arcsec/yr and 51.546 ±0.168 arcsec/yr, which are lower than the 51.749316 and 51.992344 arcsec/yr indicated by the La2004 model. Meyers and Malinverno (2018) estimated p = 51.280910 ±0.515371 arcsec/yr from a* (red/green color

reflectance) proxy data measured on the same drill core at Site 1262, and using Bayesian inversion of p and g_1 to g_5 from the precession index and orbital eccentricity bands of the data (henceforth "MM2018"). The MM2018 estimate of p is significantly lower than the La2004 model, but overlaps with our estimate. Zeebe and Lourens (2022) estimated p from the same a* time series first by fitting the time series to precession models calculated over a range of relative tidal dissipation and dynamical ellipticity parameters with the ZB18a orbital solution (Zeebe and Lourens, 2019), then estimating p with two different approaches averaging to 51.615 arcsec/yr with an undetermined uncertainty.

The cyclostratigraphic determinations of p from Sites U1410 and 1262 lead to an EMD of 383710 ± 90 km and 382625 ±265 km, and a LOD of 23.6790 ±0.0115 hours and 23.6667 ±0.0390 hours at respectively 42.5 Ma and 54.95 Ma (**Fig. 6b,c**).

4. Discussion

4.1 Uncertainties

The uncertainties of the individual Milankovitch lines are based on statistical Cramér-Rao lower bound estimates and are likely to be much larger in reality. For Site 1262, in the light of the somewhat poor resolution of the precession index lines and short duration (1700 kyr) of the reconstructed time series, it is not surprising that the p uncertainty is larger than for the twice-as-long (3423 kyr) Site U1410. The larger MM2018 uncertainty on p is governed by other assumptions, e.g., a constant sedimentation rate of 1.316 cm/kyr over the analyzed interval (2799.0 cm length; 2126.9 kyr estimated duration), filter definition, and number of parameters to fit, as well as analysis of a different proxy, i.e., a* versus the log(Fe/Ca) proxy in this study. Nonetheless, the MM2018 methodology constrains its estimates by simultaneously fitting to 12 parameters (given prior distributions), most of which are mathematically related to each other (e.g., $k+g_i$, g_i-g_j). Thus, MM2018 likely provides the more robust and conservative estimate of uncertainty on p, in which case observed p is only marginally lower than the p predicted by the precession models in **Figure 6A**.

4.2 Observation-model comparison

The cyclostratigraphically inferred Eocene estimates of p from Sites U1410 and 1262 are lower than those of the La2004 precession model (**Fig. 6**). In particular, the 54.95 Ma data estimate is significantly lower, 51.546 ±0.168 arcsec/yr, than the 51.992344 arcsec/yr indicated by the La2004 model. Meyers and Malinverno (2018) deduced an even lower p of 51.280910 ± 0.515371 arcsec/yr from the a* proxy at the same Site 1262 at 54.95 Ma. The La2004

precession model takes into account the main dissipative effects from the Earth-Moon-Sun tides (Laskar et al., 2004). These parameters do not depend on icehouse or greenhouse (ice-free) conditions. The model does not include the effects of climate friction on Earth's rotation rate caused, for example, by ice loading and unloading of the surface Earth. The discrepancy in p at 54.95 Ma between the cyclostratigraphic observations and La2004 precession model leads us to consider additional contributing factors on changes in tidal dissipation and dynamical ellipticity.

4.3. Tidal dissipation

The tidal dissipation equation describes the Earth's loss of rotational energy in response to tidal torques originating from the Moon, and can be expressed as a function of the Moon's recession rate da_M/dt (Equation 4.151 of Murray and Dermott, 1999):

$$D = \frac{1}{2}\frac{m_M m_E}{(m_M+m_E)} n a_M (\phi - n)\frac{da_M}{dt} \qquad \text{Eq. 3}$$

where the variables are as defined previously in Equation 1, and n is the mean motion of the Moon (specific values are shown in **Supplemental Material**). A present-day lunar recession rate of 3.82 cm/yr has been determined by LLR, and when applied to this equation yields a tidal dissipation rate of 3.1579 TW, which is slightly lower than 3.508 TW determined from space geodesy (Egbert and Ray, 2003), 3.54 TW determined from an expanded model with solar dissipation (Na and Lee, 2014), and 3.67 TW from model with explicit orbital elements and tidal constituents (Daher et al., 2021). In **Figure 7A**, the LLR-determined D is shown together with D obtained using EMD and ϕ estimated for Sites U1410 and 1262 (**Table 5**), compared with other estimates.

Global tidal modeling indicates M2 tidal dissipation energy of 1.4 TW for the early Eocene compared with present-day (modeled) M2 tidal dissipation energy of 2.8 TW, i.e., only 51.8% of the present-day (Green and Huber, 2013) (**Fig. 7A**). When and how, since 55 Ma, global tidal dissipation increased to its present-day value was addressed by modeling the M2 tide for intervening time slices in the Miocene (25 Ma; 2.2 TW; 79% present-day) and Pliocene (3.0 Ma; 2.4 TW; 86% present-day), which taken together indicate a strong post-Pliocene acceleration in dissipation (Green et al., 2017). The widely spaced D estimates from U1410 and 1262 cannot resolve the post-3 Ma acceleration, it does indicate that at 50 Ma, D was extremely low, much lower than even the modeled M2 tidal dissipation (**Fig. 7A**).

Over 0-25 Ma, Pälike and Shackleton (2000) determined that tidal dissipation remained close to the present-day value (T_d = 0.945 to 1.025, i.e., -5.5% to 2.5%, where T_d = 1 is the present day value), on the basis of ODP Site 926 cyclostratigraphy (equatorial western Atlantic Ocean). However, Lourens et al. (2001) found that in Pliocene cyclostratigraphy from ODP Site 967 (eastern Mediterranean Sea) from 2.45 Ma to 2.88 Ma, T_d was 50% lower than its present-day value (T_d = 0.5). Assuming present-day dynamical ellipticity (E_d =1), Zeeden et al. (2014) found that, from Miocene cyclostratigraphy at Monte dei Corvi (Ancona, Italy), T_d ranged from 0.95 to 1.05 for 9 Ma to 9.6 Ma, and from 0.95 to 1.15 for 11.5 Ma to 12.1 Ma. Also assuming present-day dynamical ellipticity, Hüsing et al. (2007) estimated T_d as 1.2 from 8.5 Ma to 12.5 Ma in the same Monte dei Corvi section, but based on visually fitting stratigraphic patterns to a selection of La2004 $(1, T_d)$ solutions.

The results from Site U1410 support the conclusion that the present-day level of tidal dissipation was maintained over 0-25 Ma; the 50% level proposed for Site 967 at 3 Ma is in conflict with results from Site 926. Re-evaluation of both Sites 967 and 926 at ~3 Ma is needed, with additional data from other sites highly desirable. The extremely low D value estimated at 50 Ma from Sites U1410 and 1262 also needs to be tested in more detail jointly with a model for dynamical ellipticity, and with additional data.

4.4 Dynamical ellipticity

The variation of dynamical ellipticity H relative to its present-day value H_0, denoted as $\delta H/H_0$, is caused by the redistribution of mass within Earth's three principal moments of inertia (Mitrovica et al., 1997). Thus, present-day $\delta H/H_0$ is equal to 0. Increased dynamical ellipticity relative to the present-day gives $\delta H/H_0 > 0$; and decreased dynamical ellipticity relative to present-day gives $\delta H/H_0 < 0$. Typical values of $\delta H/H_0$ are in the ±0.5 % range, i.e., E_d = 1.0000 ± 0.0050. Significantly, small changes in H produce large changes in p.

Over 0-25 Ma, Pälike and Shackleton (2000) found that $\delta H/H_0$ was between -0.04% and +0.01% (E_d= 0.9996 to 1.0001). Lourens et al. (2001) found that $\delta H/H_0$was 0 (E_d= 1) at 3 Ma. Zeeden et al. (2014) did not evaluate variable dynamical ellipticity in the Miocene cyclostratigraphy at Monte dei Corvei, (i.e., E_d= 1 was maintained) in favor of estimating sedimentation rate uncertainties (± 0.8 kyr for 9 Ma to 9.6 Ma, and +4 kyr/-1 kyr for 11.5 Ma to 12.1 Ma).

Estimated $\delta H/H_0$ values for Sites U1410 and 1262 are much lower than predicted by the La2004 precession model incorporating hydrostatic H (**Fig. 6B**). On the one hand if true tidal

dissipation during the Eocene was much higher than estimated by D (**Table 5**), as suggested by M2 tidal models (Green et al., 2017; Daher et al., 2021) (**Fig. 7A**), a higher tidal dissipation would require a faster lunar recession rate from 54.95 Ma to 42.5 Ma. This in turn would require, if angular momentum is to be conserved, smaller reductions of p, H, and ϕ from 54.95 Ma to 42.5 Ma. On the other hand if the p estimates indicated by Sites U1410 and 1262 are accurate, there could be forcing from unaccounted perturbations in H. Below we discuss potential effects on H from mass redistribution due to mantle convection and/or climate friction.

4.4.1 Mantle convection

Cyclostratigraphic estimates for $\delta H/H_0$ (**Fig. 7B**), owing to their different observational time windows, lead to opposing conclusions about lower mantle viscosity (weak over 0-3 Ma; rigid over 0-25 Ma) (Morrow et al., 2012). One way to resolve this "enigma" is explicit modeling of mantle convection over time given changing surface loading conditions, e.g., from sea level/glaciation changes. Recent modeling (Ghelichkhan et al., 2021) suggests that over the past 50 Ma, mantle convection increased $\delta H/H_0$= -0.2% at 50 Ma to $\delta H/H_0$= +0.2% at 20 Ma, which then subsequently decreased, gaining high frequency variations in $\delta H/H_0$ on the order of ±0.1% from the Quaternary glaciation-deglaciation cycles (2.6 Ma to present).

Of relevance to the present work is the modeled $\delta H/H_0$ of -0.2% at 50 Ma (**Fig. 7B**). This value implies a decreased p relative to that estimated by the La2004 precession model at 50 Ma; i.e., this mantle-imposed lower H subsumes the hydrostatic increase in H from the tidally enforced faster rotation rate at 50 Ma, resulting in an effective H of 0.003326623 and p=51.716018 arcsec/yr instead of the higher p=51.812434 arcsec/yr predicted for 50 Ma by the La2004 precession model (**Fig. 6A**) (details in **Supplemental Material**). If mantle convection further diminished $\delta H/H_0$ five million years earlier, i.e., at 55 Ma, this would indicate an even lower p, which would be consistent with the cyclostratigraphic estimates at Site 1262. This is "predicted" by both Sites U1410 and 1262: their estimated p values (**Fig. 6A**) can be used to identify the corresponding modeled hydrostatic $\delta H/H_0$ values, which occur at 39 Ma and 40 Ma, respectively, and indicate a total $\delta H/H_0$ that is significantly lower than predicted for 42.5 Ma and 55 Ma (**Fig. 7B**).

4.4.2 Climate friction

Deviations in p during the Late Quaternary ice ages have been modeled using sea level curves as surface loading proxies (e.g., Mitrovica et al., 1997). The modeling indicates lower $\delta H/H_0$ during glacials and higher $\delta H/H_0$ during interglacials, consistent with water masses moving toward the poles during glacials, and toward the equator during interglacials, yielding an increase in p with an increase in $\delta H/H_0$. While this has been modeled with increased complexity over the years (e.g., Ghelichkhan et al., 2021; Farhat et al., 2022), there is as yet no observational confirmation for this result. However, there are reports for unexpected behavior in Milankovitch cycles recorded much further back in time that might be related to this climate friction. Mitchell et al. (2021) suggested that during snowball earths rapid decreases in p and rotation rate (and increased LOD) may have occurred with the transfer of water from the poles to equatorial regions.

However, the early Eocene Epoch was a time of severe global warmth, with little to no ice at either of the poles (e.g., Zachos et al., 2001; Westerhold et al., 2020). Therefore, climate-induced $\delta H/H_0$ variations with a magnitude on the order of that predicted for Quaternary ice dynamics are unlikely – variations would be much smaller. In the early Eocene, the high global temperature generated an accelerated hydrological cycle and associated climate and ocean processes, i.e., continental weathering, sea-level, and ocean circulation (e.g., Bice and Marotzke, 2001; Zachos et al., 2005; Nunes and Norris, 2006; Penman et al., 2015). In particular, a reorganization in ocean circulation occurred during the PETM with water mass transfer and redistribution between the Northern and Southern hemispheres (e.g., Bice and Marotzke, 2001; Nunes and Norris, 2006) in a manner similar to that modeled for present-day warming (Landerer et al., 2007). The earliest Eocene also witnessed North Atlantic rifting and the onset of the North Atlantic Igneous Province (Zachos et al., 2001). All of these changes to Earth's surface may have measurably contributed to the dynamical ellipticity.

Evidence for a potential discrepancy in the LOD between the model (2.3 ms/century) and observations (1.8 ms/century) has been shown during the past ~2700 years, suggesting extra non-tidal effects on Earth's rotation rate, e.g., change in the dynamical ellipticity induced by mantle response to post-glacial rebound, which are not taken into account in the model (Stephenson et al., 2016). Present-day global warming has also been shown as a potential contributor for the discrepancy between the model and observations, by changing atmosphere-ocean circulations and water redistribution between deep- and shallow-marine environments (de Viron et al., 2002; Landerer et al., 2007). Although all the above suggested forcing processes on Earth's rotation rate are not yet well known, future studies should further

investigate on specific forcing factors for a better comprehension of the evolution of Earth's rotational and precessional dynamics.

5. Conclusions

The Eocene Epoch may be the most recent geologic period where effects from the Earth-Moon dynamical parameters can be unambiguously distinguished in recorded Milankovitch cycles. The main problem is the presence of variations in sedimentation rate at Milankovitch time scales, and the degree of success in measuring and attenuating their effects. Recent improvements in the acquisition of high-resolution stratigraphic proxies such as those analyzed here, and careful tuning to stable astronomical metronomes, are sufficient to detect Milankovitch lines in cyclostratigraphy with adequate certainty, and to estimate the Earth-Moon dynamical parameters. In summary:

- Eocene cyclostratigraphy of IODP Site U1410 (40.9-44.3 Ma) and ODP Site 1262 (54.1-55.8 Ma) in the Atlantic Ocean provides constraints on Earth-Moon dynamical parameters.
- Multi-taper harmonic line analysis with data-adaptive weighting was used to identify obliquity lines $p+s_3$ and $p+s_4$ at Site U1410, and precession index lines $p+g_2$ and $p+g_3$ at Site 1262.
- Each line frequency and its Cramér-Rao lower bound uncertainty were used to reconstruct Earth's precession frequency, length-of-day and Earth-Moon distance, assuming an existing model of Solar System frequencies and uncertainties for s_3, s_4, g_2 and g_5.
- Observed p at 42.5 Ma (Site U1410) is 51.486 ± 0.064 arcsec/yr, and at 54.95 Ma (Site 1262) is 51.546 ± 0.168 arcsec/yr, which deviates from constant tidal dissipation precession model based upon the present-day dissipation rate, more so at 54.95 Ma, then converging toward the model at 42.5 Ma.
- The results at 54.95 Ma (Site 1262) are consistent with previous studies that investigated different proxy data from the same Site 1262 drill core with different methods of analysis and modeling.
- The discrepancy in p between the observations and La2004 theoretical precession model at 54.95 Ma point to a significantly lower Eocene tidal dissipation rate (an order of magnitude lower than present-day) and additional impacts from changes in Earth's dynamical ellipticity from mantle convection and potentially global warming.

Declaration of Competing Interest

The authors declare that they have no known competing financial interests or personal relationships that could have appeared to influence the work reported in this paper.

Acknowledgments

S. Boulila has been supported by the French Agence Nationale de la Recherche (AstroMeso ANR-19-CE31-0002-01), and the European Research Council (ERC) under the European Union's Horizon 2020 research and innovation program (Advanced Grant AstroGeo-885250). L.A. Hinnov is grateful to the Heising-Simons Foundation for generous support of the CycloAstro Project, Grant # 2021-2796. This research used samples and data provided by the International Ocean Discovery Program (IODP). S.B. is grateful to IODP France for a previous support. We thank reviewers H. Davies, J. Laurin, and an anonymous reviewer, for their detailed comments and insights, which led to key improvements to the paper.

Appendix A. Supplementary material to this article can be found online at .....

Code availability. MATLAB scripts used in this study can be found at ....

References

Archer, A.W., 1996. Reliability of lunar orbital periods extracted from ancient cyclic tidal rhythmites. Earth Planet. Sci. Lett. 141, 1–10.

Berger, A., Loutre, M., Laskar, J., 1992. Stability of the astronomical frequencies of the Earth's history for paleoclimate studies. Science 255, 560–566.

Berger, A., Loutre, M.-F., Dehant, V., 1989. Influence of the changing lunar orbit on the astronomical frequencies of pre-Quaternary insolation patterns. Paleoceanography 4(5), 555–564.

Bice, K.L., Marotzke, J., 2001. Numerical evidence against reversed thermohaline circulation in the warm Paleocene/Eocene ocean. J. Geophys. Res. 106, 11529–11542.

Bohaty, S.M., Zachos, J.C., 2003. Significant Southern Ocean warming event in the late middle Eocene. Geology 31(11), 1017– 1020.

Boulila, S., 2019. Coupling between Grand cycles and Events in Earth's climate during the past 115 million years. Science Reports 9, 327.

466 Boulila, S., Vahlenkamp, M., De Vleeschouwer, D., Laskar, J., Yamamoto, Y., Pälike, H.,
467 Kirtland Turner, S., Sexton, P.F., Cameron, A., 2018. Towards a robust and consistent
468 middle Eocene astronomical timescale. Earth and Planetary Science Letters 486, 94–107.
469 Boulila, S., Galbrun, B., Huret, E., Hinnov, L.A., Rouget, I., Gardin, S., Bartolini, A., 2014.
470 Astronomical calibration of the Toarcian Stage: implications for sequence stratigraphy
471 and duration of the early Toarcian OAE. Earth and Planetary Science Letters 386, 98–
472 111.
473 Brosche, P. Sündermann, J., 1978. Tidal Friction and the Earth's Rotation I, Springer-Verlag,
474 Berlin, 242 p.
475 Coughenour C.L., Archer A.W., Lacovera K.J., 2009. Tides, tidalites, and secular changes in
476 the Earth-Moon system. Earth Sci Rev. 97, 59–79.
477 Daher, H., and 17 others, 2021. Long-term Earth-Moon evolution with high-level orbit and
478 ocean tide models. Journal of Geophysical Research, Planets, 126, e2021JE006875.
479 Deubner, F.-L., 1990. Discussion on Late Precambrian tidal rhythmites in South Australia and
480 the history of the Earth's rotation, Journal of the Geological Society, London 147, 1083–
481 1084.
482 de Viron, O., Dehant, V., Goosse, H., Crucifix, M., and participating CMIP modeling groups,
483 2002. Effect of global warming on the length-of-day. Geophys. Res. Lett. 29(7), 1146,
484 doi:10.1029/2001GL013672.
485 Dickey, J.O., Bender, P.L., Faller, J.E., Newhall, X.X., Ricklefs, R.L., Ries, J.G., Shelus, P.J.,
486 Veillet, C., Whipple, A.L., Wiant, J.R., Williams, J.G., Yoder, C.F., 1994. Lunar laser
487 ranging: a continuing legacy of the Apollo Program. Science 265, 482–490.
488 Egbert, G.D., Ray, R.D., 2003. Semi-diurnal and diurnal tidal dissipation from
489 TOPEX/Poseidon altimetry. Geophysical Research Letters, 30(17), 1907.
490 Farhat, M., Laskar, J., Boué, G., 2022. Constraining the Earth's Dynamical Ellipticity from Ice
491 Age Dynamics. Journal of Geophysical Research, 127, e2021JB023323.
492 Forte, A.M., Mitrovica, J.X., 1997. A resonance in the Earth's obliquity and precession over
493 the past 20 Myr driven by mantle convection. Nature 390, 676–680.
494 Ghelichkhan, S., Fuentes, J.J., Hoggard, M.J., Richards, F.D., Mitrovica, J.X., 2021. The
495 precession constant and its long-term variation. Icarus, 358, 114172.
496 Green, J.A.M., Huber, M., Waltham, D., Buzan, J., Wells, M., 2017. Explicitly modelled deep-
497 time tidal dissipation and its implication for Lunar history. Earth and Planetary Science
498 Letters 461, 46–53.

499 Green, J.A.M., Huber, M., 2013. Tidal dissipation in the early Eocene and implications for
500 ocean mixing, Geophysical Research Letters 40, 2707–2713.
501 Gradstein, F.M., Ogg, J.G., Schmitz, M.D., Ogg, G., 2020. Geological Time Scale 2020.
502 Elsevier, Amsterdam.
503 Hüsing, S.K., Hilgen, F.J., Abdul Aziz, H., Keijgsman, W., 2007. Completing the Neogene
504 geological time scale between 8.5 and 12.5 Ma. Earth and Planetary Science Letters 253,
505 340–358.
506 Kvale, E.P., 2012. Tidal Constituents of Modern and Ancient Tidal Rhythmites: Criteria for
507 Recognition and Analyses. In Davis, Jr., R.A., and Dalrymple, R.W., (eds.), Principles of
508 Tidal Sedimentology, Springer Science, 1-17.
509 Lambeck, K., 1980. The Earth's Variable Rotation: Geophysical Causes and Consequences.
510 Cambridge University Press, New York, 449 p.
511 Landerer, F.W., Jungclaus, J.H., Marotzke, J., 2007. Ocean bottom pressure changes lead to a
512 decreasing length-of-day in a warming climate. Geophys. Res. Lett. 34, L06307.
513 Laskar, J, 2020. Chapter 4: Astrochronology, in Gradstein, F, Ogg, J, Schmitz, M, Ogg, G, eds,
514 Geologic Time Scale 2020, Elsevier, Amsterdam, 139–158.
515 Laskar, J., Robutel, P., Joutel, F., Gastineau, M., Correia, A.C.M., Levrard, B., 2004. A long-
516 term numerical solution for the insolution quantities of the Earth. Astronomy and
517 Astrophysics 428, 261–285.
518 Lourens, L.J., Wehausen, R., Brumsack, H.J., 2001. Geological constraints on tidal dissipation
519 and dynamical ellipticity of the earth over the past three million years. Nature 409, 1029–
520 1033.
521 Li, M., Huang, C., Hinnov, L.A., Chen, W., Ogg, J.G., Tian, W., 2018. Astrochronology of the
522 Anisian stage (middle Triassic) at the Guandao reference section, south China. Earth and
523 Planetary Science Letters 482, 591–606.
524 Li, M., Huang, C., Hinnov, L.A., Ogg, J., Chen, Z.-Q., Zhang, Y., 2016. Obliquity-forced
525 climate during the early triassic hothouse in China. Geology 44, 623–626.
526 Liu, W., Wu, H., Hinnov, L.A., Xi, D., He, H., Zhang, S.,Yang, T., 2020. Early Cretaceous
527 Terrestrial Milankovitch Cycles in the Luanping Basin, North China and Time
528 Constraints on the Early Stage Jehol Biota. Frontiers in Earth Science 8, 178.
529 McCarthy, D.D., Seidelmann, P.K., 2018. Time: From Earth Rotation to Atomic Physics, 2nd
530 Edition, Cambridge University Press, Cambridge, UK.
531 Meyers, S.R., Malinverno, A., 2018. Proterozoic Milankovitch cycles and the history of the
532 solar system. Proceedings of the National Academy of Sciences 115(25), 6363–6368.

Mitchell, R.N., Gernon, T.M., Cox, G.M., Nordsvan, A.R., Kirsher, U., Xuan, C., Liu, Y., Liu, X., He, X., 2021. Orbital forcing of ice sheets during snowball Earth. Nature Communications 12, 4187.

Mitrovica, J.X., Forte, A.M., Pan, R., 1997. Glaciation-induced variations in the Earth's precession frequency, obliquity and insolation over the last 2.6 Ma. Geophysical Journal International 128, 270–284.

Mitrovica, J.X., Hay, C.C., Morrow, E., Kopp, R.E., Dumberry, M., Stanley, S., 2015. Reconciling past changes in Earth's rotation with 20th century global sea-level rise: Resolving Munk's enigma. Science Advances 1, e1500679.

Morrow, E., Mitrovica, J.X., Forte, A.M., Glisovic, P., Huybers, P., 2012. An enigma in estimates of the Earth's dynamic ellipticity. Geophysical Journal International 191, 1129–1134.

Murphy, T.W., 2013. Lunar laser ranging: the millimeter challenge. Rep. Prog. Phys. 76, 076901.

Murray, C.D., Dermott, S.F., 1999. Solar System Dynamics, Cambridge University Press, Cambridge, 591 p.

Na, S-H, 2013. Chapter 9: Earth Rotation – Basic Theory and Features, Geodetic Science, Intechopen.

Na, S.-H., Lee, S., 2014. Re-estimation of Earth spin rotational energy decrease due to tidal friction. Geosciences Journal, 18(1), 1-6.

Nunes, F., Norris, R.D., 2006. Abrupt reversal in ocean overturning during the Palaeocene/Eocene warm period. Nature 439, 60–63.

Pälike, H., Shackleton, N.J., 2000. Constraints on astronomical parameters from the geological record for the last 25 Myr. Earth and Planetary Science Letters 182, 1–14.

Paillard, D., Labeyrie, L., Yiou, P., 1996. Macintosh program performs timeseries analysis. Eos, 77, 379.

Park, J.J., Lindberg, C.R., and Vernon III, F.L., 1987. Multitaper spectral analysis of high-frequency spectrograms, Journal of Geophysical Research 92, 12675-12684.

Penman, D.E., Kirtland Turner, S., Sexton, P.F., Norris, R.D., Dickson, A.J., Boulila, S., Ridgwell, A., Zeebe, R.E., Zachos, J.C., Cameron, A., Westerhold, T., Röhl, U., 2016. An abyssal carbonate compensation depth overshoot in the aftermath of the Palaeocene-Eocene Thermal Maximum. Nature Geoscience 9, 575–580.

Rosenberg, GD, Runcorn, SK, 1975. Growth Rhythms and the History of the Earth's Rotation. Wiley, London, 559 p.

567 Runcorn, S. K., 1979. Palaeontological data on the history of the Earth-Moon system, Phys.
568 Earth Planet. Inter. 20, 1–5.
569 Stephenson, F.R., Morrison, L.V., Hohenkerk, C.Y., 2016. Measurement of the Earth's
570 rotation: 720 BC to AD 2015. Proc. R. Soc. A 472: 20160404.
571 Thomson, D.J., 2009. Time series analysis of paleoclimate data, in Gornitz, V., ed.,
572 Encyclopedia of Paleoclimatology and Ancient Environments, Encyclopedia of Earth
573 Sciences Series, Springer, Dordrecht, 949–959.
574 Thomson, D.J., 1990. Quadratic-Inverse Spectrum Estimates: Applications to
575 Palaeoclimatology, Philosophical Transactions: Physical Sciences and Engineering
576 332(1627), 539–597.
577 Thomson, D.J., 1982. Spectrum estimation and harmonic analysis. IEEE Proceedings 70, 1055–
578 1096.
579 Walker, J.C.G., Zahnle, K.J., 1986. Lunar nodal tide and distance to the Moon during the
580 Precambrian. Nature 320, 600–602.
581 Waltham, D., 2015. Milankovitch period uncertainties and their impact on cyclostratigraphy,
582 Journal of Sedimentary Research 85, 990–998.
583 Westerhold, T., Marwan, N., Drury, A.J., Liebrand, D., Agnini, C., Anagnostou, E., Barnet,
584 J.s.k., Bohaty, S.M., De Vleeschouwer, D., Florindo, F., Frederichs, T., Hodell, D.A.,
585 Holbourn, A.E., Kroon, D., Lauretano, V., Littler, K., Lourens, L., Lyle, M., Pälike, H.,
586 Röhl, U., Tian, J., Wilkins, R.H., Wilson, P.A., Zachos, J.C., 2020. An astronomically
587 dated record of Earth's climate and its predictability over the last 66 million years.
588 Science 369, 1383–1387.
589 Westerhold, T., Röhl, U., Laskar, J., Bowles, J., Raffi, I., Lourens, L.J., Zachos, J.C., 2007. On
590 the duration of magnetochrons C24R and C25n and the timing of early Eocene global
591 warming events: implications from the Ocean Drilling Program Leg 208 Walvis Ridge
592 depth transect. Paleoceanography 22, PA2201.
593 Williams, G.E., 2000. Geological constraints on the Precambrian history of Earth's rotation.
594 Rev. Geophys. 38 (1), 37–59.
595 Williams, J.G., Turyshev, S.G., Boggs, D.H., 2014. The past and present Earth-Moon system:
596 the speed of light stays steady as tides evolve. Planetary Science 3(2), doi:
597 10.1186/s13535-014-0002-5.
598 Wu, H., Zhang, S., Hinnov, L.A., Feng, Q., Jiang, G., Li, H., Yang, T., 2013. Late Permian
599 Milankovitch cycles. Nat. Commun. 4, 3452.

Wu, H., Fang, Q., Wang, X., Hinnov, L.A., Qi, Y., Shen, S., Yang, T., Li, H., Chen, J., Zhang, S., 2019. A ~34 m.y. astronomical time scale for the uppermost Mississippian through Pennsylvanian of the Carboniferous System. Geology, 47(1), 83–86.

Zachos, J.C., Pagani, M., Sloan, L., Thomas, E., Billups, K., 2001. Trends, rhythms, aberrations in global climate 65 Ma to present. Science 292, 686–693.

Zachos, J.C. et al., 2005. Rapid acidification of the ocean during the Paleocene-Eocene thermal maximum. Science 308, 1611–1615.

Zeebe, R.E., Lourens, L.J., 2022. A deep-time dating tool for paleo-applications utilizing obliquity and precession cycles: The role of dynamical ellipticity and tidal dissipation, Paleoceanography and Paleoclimatology 37, e2021PA004349.

Zeebe, R.E., Lourens, L.J., 2019. Solar system chaos and the Paleocene-Eocene boundary age constrained by geology and astronomy. Science 365 (6456), 926–929.

Zeeden, C., Hilgen, F.J., Hüsing, S.K., and Lourens, L.L., 2014. The Miocene astronomical time scale 9–12 Ma: New constraints on tidal dissipation and their implications for paleoclimatic investigations. Paleoceanography 29, 296–307.

Tables

Table 1. Astronomical forcing of Earth's insolation involves p modulated by the fundamental frequencies g_i and s_i of the planets: $p+s_i$ for obliquity, and $p+g_i$ for precession index, i = 1, 2, …, 8 (the planets in order of distance from the Sun), where (in arcsec/year) s_3 = -18.845166, s_4 = -17.758310, g_1 = 5.579378, g_2 = 7.456665, g_3 = 17.366595, and g_5 = 4.257564 (Tables 4 and 5 in Laskar et al., 2004). Values of p are according to Equation 40 in Laskar et al. (2004).

Variable	Present-day	42.5 Ma	54.95 Ma
p (arcsec/year)	50.475838	51.636043	51.990891
Obliquity lines (period in years)			
$p+s_3$	40973	39523	39100
$p+s_4$	39612	38255	37859
Precession index lines (period in years)			
$p+g_5$	23678	23187	23041
$p+g_1$	23120	22651	22512
$p+g_2$	22371	21932	21801
$p+g_3$	19103	18782	18686
$p+g_4$	18951	18635	18540

Table 2. g_i and s_i are from Tables 4 and 5 of Laskar et al. (2004), used in b in Equation 2, and σ_{gi} and σ_{si} from Δ100 in Table 3 of Laskar et al. (2004), used in σ_b in Equation 2.

g_i, s_i (arcsec/yr)	σ_{gi}, σ_{si} (arcsec/yr)
s_3 = -18.845166	σ_{s3} = 0.066
s_4 = -17.758310	σ_{s4} = 0.064
g_2 = 7.456665	σ_{g2} = 0.019
g_3 = 17.366595	σ_{g3} = 0.200

631

632

633 **Table 3**. Calculating empirical p from selected cyclostratigraphic lines. **A.** At 42.5 Ma, average
634 p of the two obliquity lines is 51.485818 ± 0.06410516777 arcsec/yr. **B**. At 54.95 Ma, average
635 p of the two precession index lines is 51.54597 ± 0.1683589717 arcsec/yr:

636

A. 42.5 Ma (mid-point age of Site U1410 s_3-s_6 tuned time series)							
line	F(f)	f (kyr')	σ_f (±kyr')	P (kyr)	σ_P (±kyr)	p (arcsec/yr)	σ_p (arcsec/yr)
p+s_3	8.114	0.02524	0.00003998	39.620	0.063	51.556206	0.08390887251
p+s_4	4.11	0.02597	0.00005618	38.506	0.083	51.415430	0.09693911106

637

B. 54.95 Ma (mid-point age of Site 1262 g_2-g_5 tuned time series)							
line	F(f)	f (kyr')	σ_f (±kyr')	P (kyr)	σ_P (±kyr)	p (arcsec/yr)	σ_p (arcsec/yr)
p+g_2	2.599	0.04571	0.00014225	21.877	0.068	51.783495	0.1853324978
p+g_3	2.269	0.05299	0.00015244	18.871	0.054	51.308445	0.2811242406

638

639

640 **Table 4**. Estimated Earth-Moon parameters for the two study sites (see **Figure 6**).

641

Parameter	Site U1410: 42.5 Ma $\pm\sigma$ *error*	Site 1262: 54.95 Ma $\pm\sigma$ *error*	Site 1262: 54.95 Ma (MM2018) $\pm\sigma$ *error*
p (arcsec/yr)	51.485818 ± 0.064105	51.545970 ± 0.168359	51.280910 ± 0.515371
ϕ (10^{-5}rads/s)	7.372315 ± 0.005	7.374420 ± 0.010	not reported
LOD (hours)	23.6790 ± 0.0115	23.6670 ± 0.0390	23.731816 ± 0.123398
H (ratio)	0.00331215 ± 0.004	0.003314043 ± 0.008	not reported
a_M (10^3 km)	382.668 ± 0.090	382.623 ± 0.265	383.110800 ± 0.822051

642

643

644 **Table 5**. Tidal dissipation estimates based on the Lunar Laser Ranging (LLR) lunar recession
645 rate and EMD estimates from Sites U1410 and 1262 (**Table 4)**. Calculation details are provided
646 in the **Supplemental Material.** These tidal dissipation values are compared with other
647 estimates in **Figure 7A**.
648

n	t (Ma)	$\phi\ (x10^{-5})$ (rad/s)	$a_M(x10^8)$ (m)	$a_{Mn-1} - a_{Mn}(x10^8)$ (m)	$t_n - t_{n-1}$ (Myr)	$\frac{da_M}{dt}$ (cm/yr)	D (TW)	midpoint t (Ma)
0	0	7.292115	3.84399	LLR	LLR	3.82	3.1579	0
1	42.5	7.372315	3.82668	0.0063	17.5	4.07	3.3901	21.25
2	54.95	7.374420	3.82623	0.00045	12.45	0.36	0.3009	48.725

649
650

Figure captions

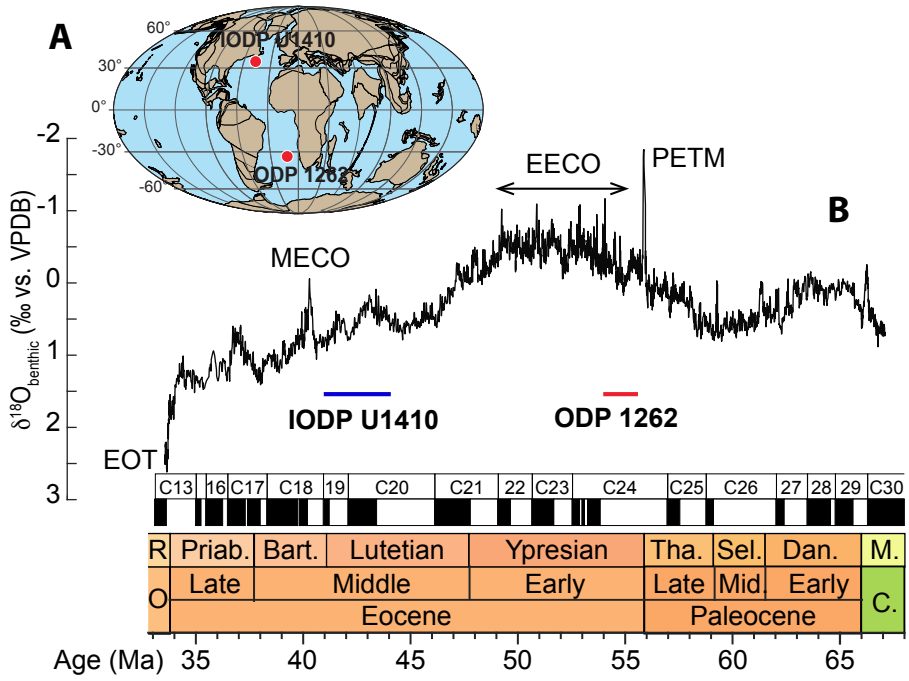

Figure 1. Study framework in the Eocene Atlantic Ocean. **A.** Paleogeographic (40 Ma) location of IODP Site U1410 (present-day: 41°19.6987' N; 49°10.1995' W) and ODP Site 1262 (present-day: 27°13.0000' S; 1°32.9833' E). **B.** Benthic foraminiferal stable oxygen isotopes of the interval from 33.5 Ma to 67.1 Ma (Westerhold et al., 2020), shown with IODP Site U1410 and ODP Site 1262 time intervals. EOT: Eocene-Oligocene transition, MECO: Middle Eocene Climate Optimum; EECO: Early Eocene Climate Optimum, PETM: Paleocene-Eocene Thermal Maximum (see Zachos et al., 2001).

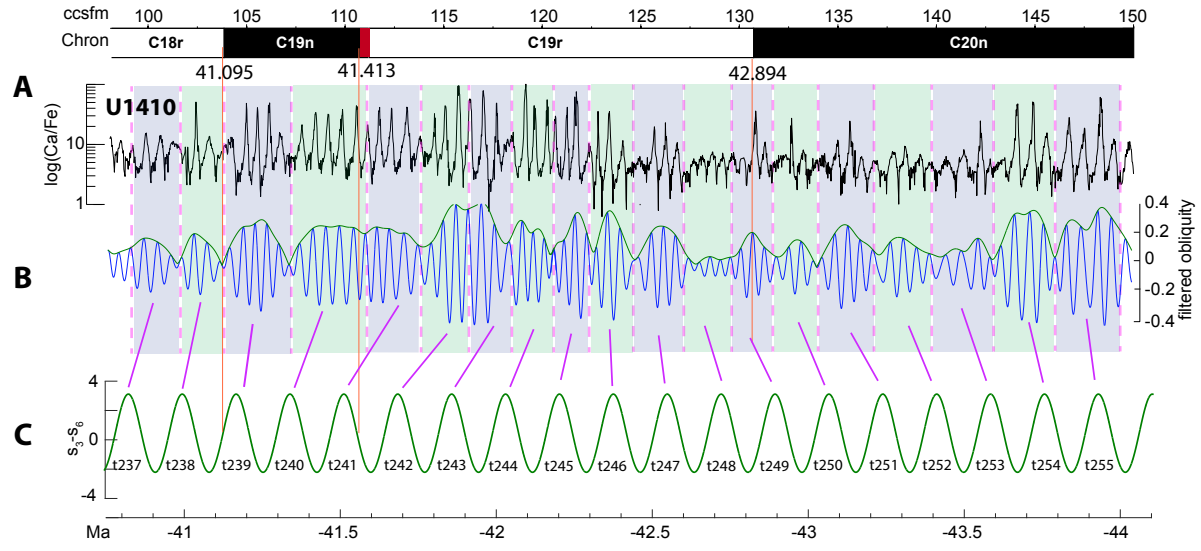

Figure 2. Integrated stratigraphy from IODP Site U1410 (40.9 Ma to 44.3 Ma, Boulila et al., 2018). **A.** Magnetostratigraphy and high-resolution (2 cm) XRF measurements of Fe/Ca counts in $\log_{10}$ scale. **B.** Amplitude modulations of obliquity-scale couplets of clay- and carbonate-rich lithologies in the core depth domain (bandpass 1.5 ±0.6 cycles/m), reinforced with purple and green shading and red-dashed vertical lines in the background. **C.** The La2011 s_3-s_6 inclination metronome (173-kyr cycle), with tie points to the obliquity modulations in the data above. Tuning to this metronome yields a time series of duration 3423 kyr. Note: basal ages of Chrons C19r, C19n, and C18r are 42.894, 41.413 and 41.095 Ma, respectively (Boulila et al., 2018) compared with 42.196, 41.180 and 41.030 Ma in GPTS2020 (Gradstein et al., 2020) (see **Supplementary Material**). ccsfm = core composite depth below seafloor.

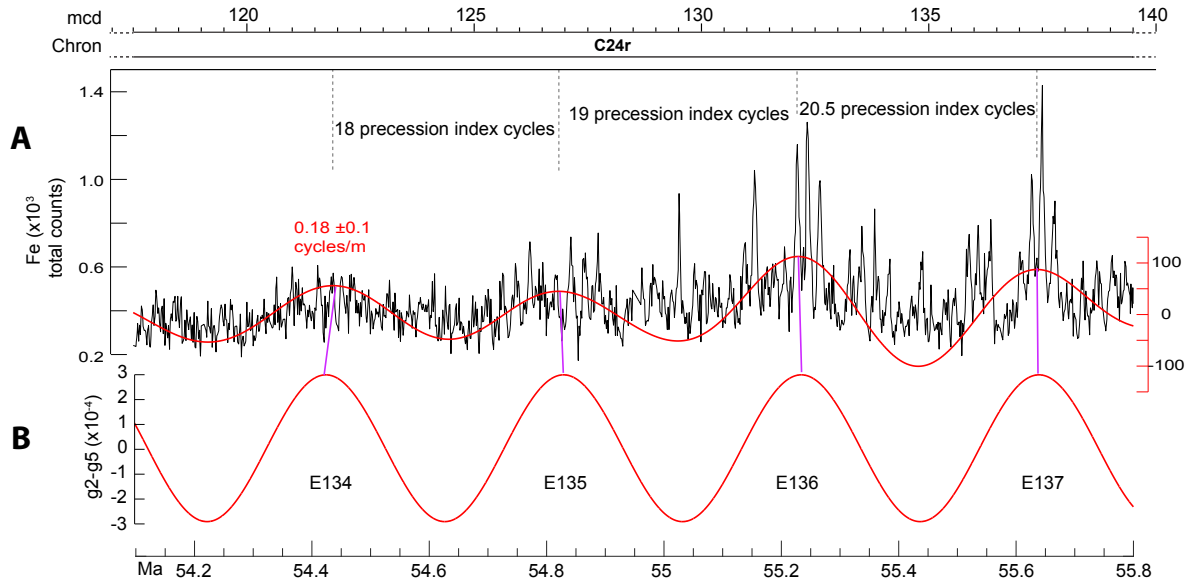

Figure 3. Integrated stratigraphy from ODP Site 1262 (54.1 Ma to 55.8 Ma, Westerhold et al., 2007). **A.** Magnetostratigraphy and high-resolution (2 cm) XRF Fe counts, shown with a ~400 kyr orbital eccentricity bandpass signal (passband: 0.18 ±0.10 cycles/m in red). **B.** La2011 g_2-g_5 eccentricity metronome (405-kyr cycle), with tie points to the bandpass signal above. Tuning to this metronome leads to a time duration of 1700 kyr for the interval. The stratigraphic positions of ELMO (ETM2) at 117 mcd and PETM at 140 mcd, i.e., just outside the studied interval, have respective ages of 54.1 Ma and 56.01 ± 0.05 Ma (Zeebe and Lourens, 2019), mcd = meters composite depth.

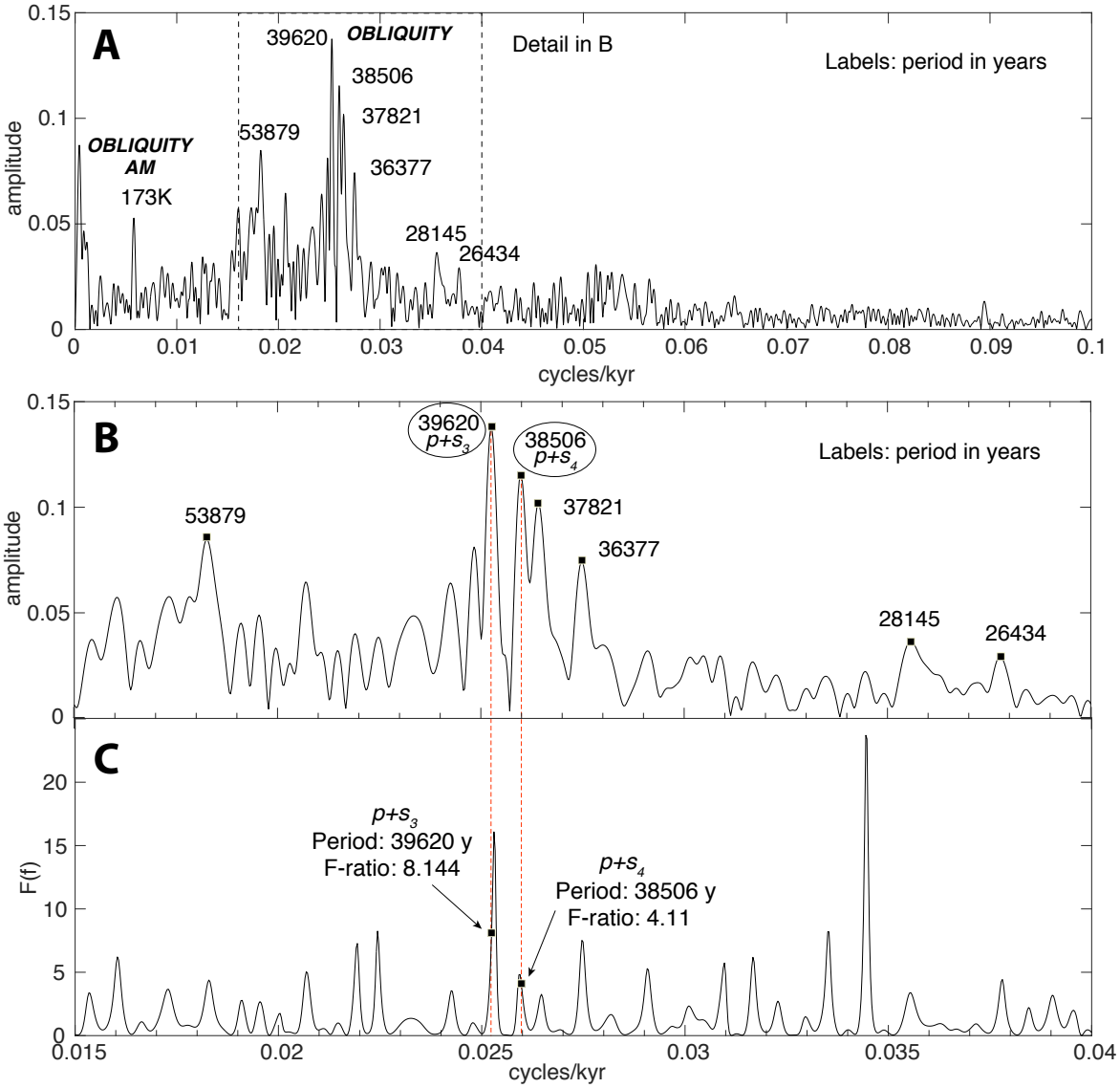

Figure 4. 2π MTM adaptive data weighted harmonic analysis of the s_3-s_6-tuned XRF Ca/Fe time series at IODP Site U1410. **A.** Line spectrum. **B.** Obliquity band of the line spectrum. **C.** Obliquity band of the F-test spectrum. $p+s_3$ and $p+s_4$ and their F-ratios are used to estimate p and uncertainties (see text and **Supplementary Material** for additional information).

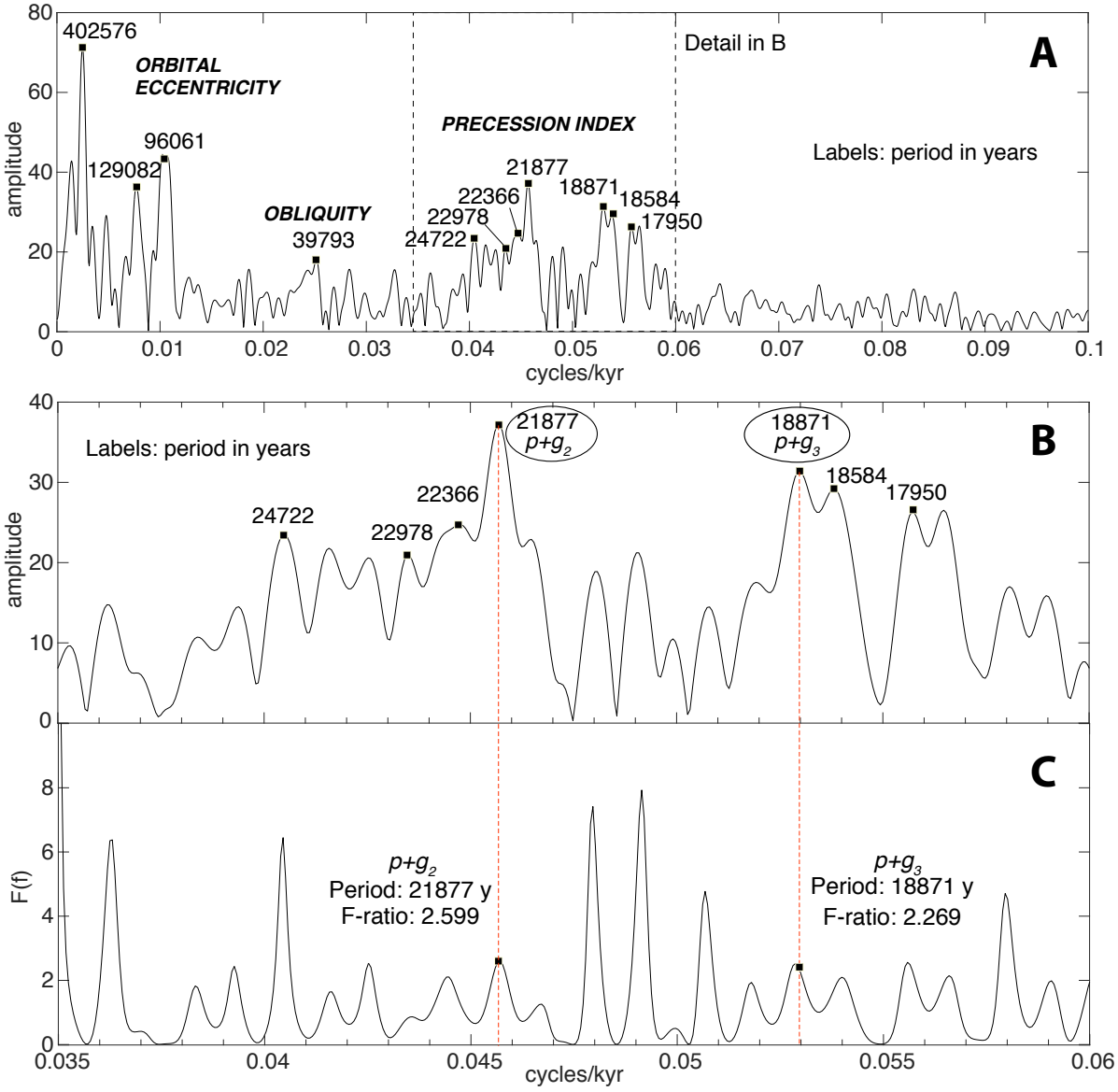

690

691 **Figure 5.** 2π MTM adaptive data weighted harmonic analysis of the g_2-g_5-tuned XRF Fe time
692 series at ODP Site 1262. **A.** Line spectrum. **B.** Precession index band of the line spectrum**. C.**
693 Precession index band of the F-test spectrum. $p+g_2$ and $p+g_3$ and their F-ratios are used to
694 estimate p and uncertainties (see text and **Supplementary Material** for additional information).
695

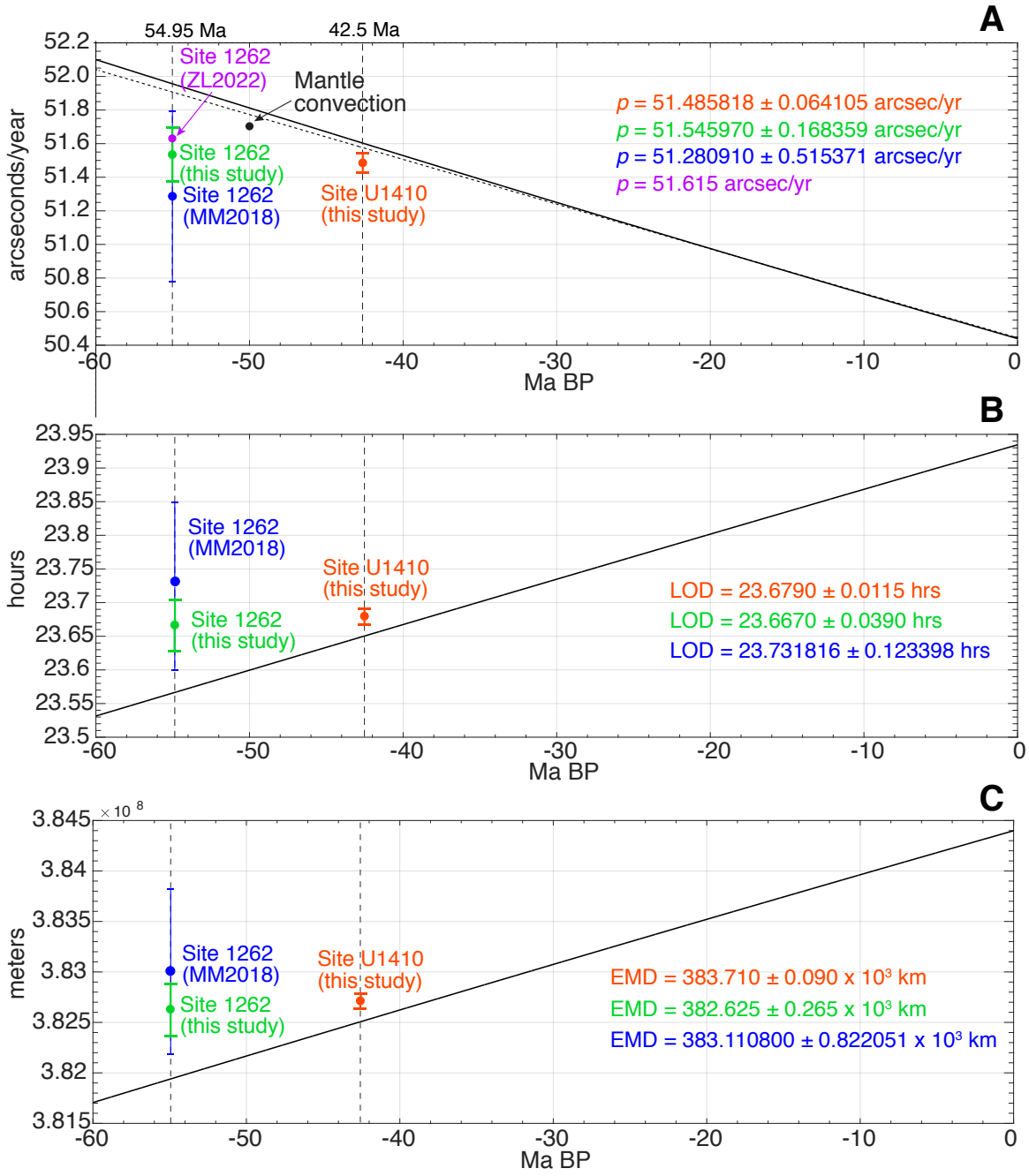

Figure 6. Eocene Earth-Moon dynamical parameters. Values for the cyclostratigraphic estimates are summarized in **Table 4**. **A.** Precession frequency (p). The solid black line is the La2004 precession model (Equation 40 of Laskar et al., 2004) computed in *earthmoonkandT_pmodel.m* (see **Supplemental Material**); the dashed black line is the linear smooth-change tidal model of Waltham (2015). The black dot labeled "Mantle convection" shows the reduction in La2004 p at 50 Ma due to mantle convection (see **Discussion**). **B.** Dynamical ellipticity ($H = H(\phi) = 6.094\ x\ 10^5\ x\ \phi^2$). **C.** Earth rotation rate ϕ. **D.** Length-of-day (LOD) in sidereal hours. **E.** Earth-Moon distance (EMD) in meters. Black line for the La2004 precession model in Panel **A** was calculated with Eq. 40 in Laskar et al. (2004),

substituting 50.439273 arcsec/yr for 50.475838 arcsec/yr, to ensure LOD of 23.9345 hours and EMD of 384,400 km at t=0 Ma in *earthmoonkandT.m* (see **Supplemental Material**). The La2004 model *p*, was then searched to identify the appropriate ϕ, H, and EMD based on conservation of angular momentum, which are recorded by the black lines in Panels **B-E**. Red text and symbols: estimates from Site U1410; green text and symbols: estimates from Site 1262; blue text and symbols: estimates from Meyers and Malinverno (2018) (MM2018) using the a* proxy from the same drill core at Site 1262; magenta text and symbol are from Zeebe and Lourens (2022), who estimated p = 51.615 arcsec/yr (no uncertainties). The uncertainties in p are projected onto the black lines to estimate the uncertainties for H, ϕ, LOD and EMD for Sites U1410 and 1262. Note: The MM2018 estimate for LOD has been adjusted from 23.804850 hours (Table 2 in Meyers and Malinverno, 2018) to 23.731816 hours (S.R. Meyers and A. Malinverno, personal communication).

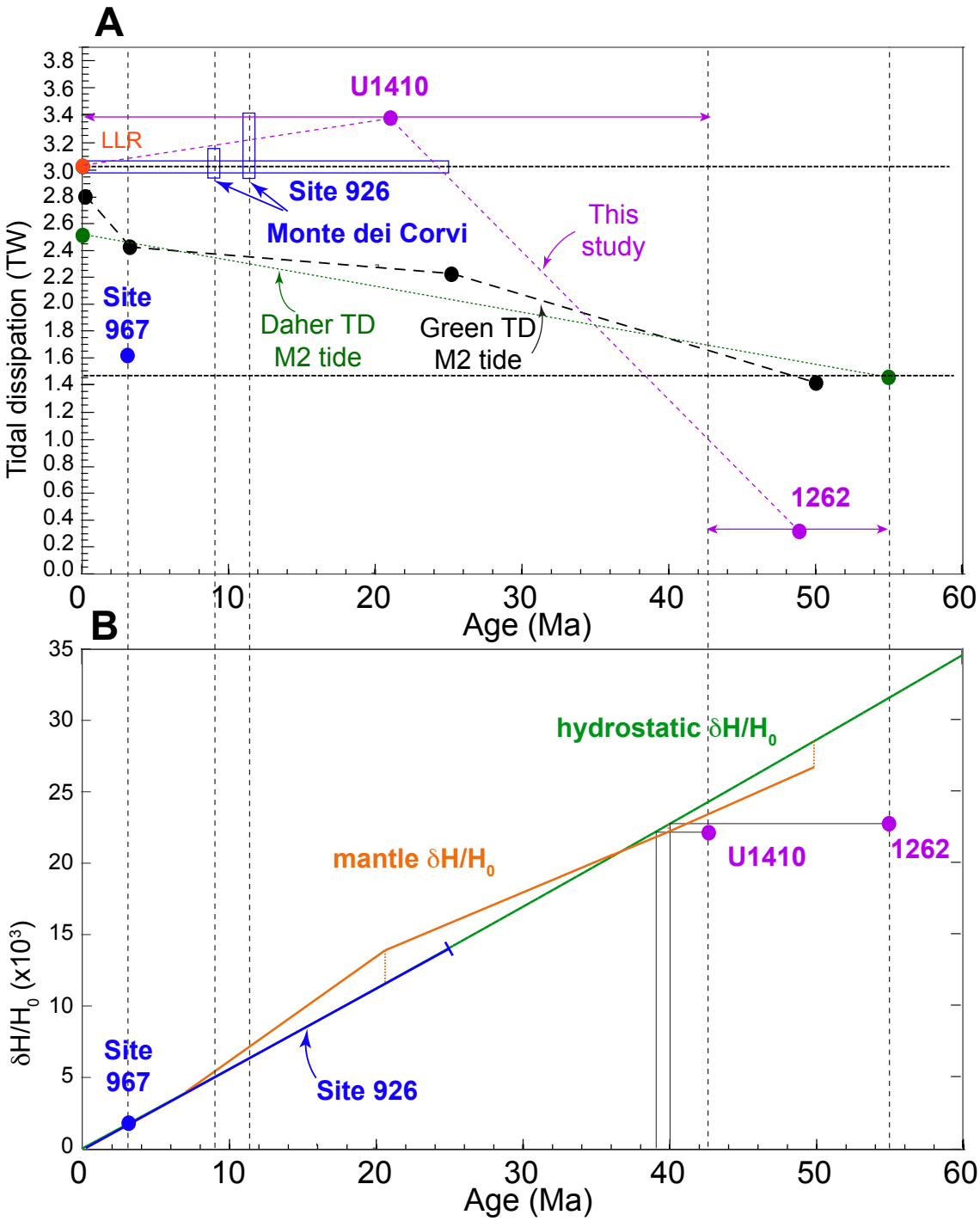

Figure 7. Principal forcing factors of *p*, 0-60 Ma. Vertical dashed lines indicate ages of cyclostratigraphy from ODP Site 967 (Lourens et al., 2001), Site 926 (Pälike and Shackleton 2000), Monte dei Corvei (Zeeden et al., 2014), and Sites U1410 and 1262 from this study, that have been measured for tidal dissipation and/or dynamical elllipticity. **A**. Tidal dissipation. Present-day (0 Ma) global tidal dissipation is estimated as 3.1579 TW from the lunar recession rate by Lunar Laser Ranging (closed red circle labeled LLR); the average tidal dissipation is estimated from the change in EMD indicated by Sites U1410 and 1262 from 0 Ma to 42.5 Ma

and from 42.5 Ma to 54.95 Ma (**Table 5**), and recorded at midpoint times of 21.25 Ma and 48.725 Ma with closed purple circles; the three estimates are connected by purple dashed lines. Present-day M2 tidal dissipation of 2.8 TW is extrapolated back in time with modeled time slices at 3 Ma, 20 Ma and 50 Ma indicated by closed black circles and connected by black dashed lines (Green et al., 2017). A more recent model of present-day M2 tidal dissipation of 2.51 TW and a modeled time slice at 55 Ma is indicated by green closed circles and connected by a green dashed line, from Daher et al. (2021). The blue closed circle indicates the cyclostratigraphic estimate from Site 967 (Lourens et al., 2001); the blue rectangles are estimates from Site 926 (Pälike and Shackleton 2000) and Monte dei Corvi (Zeeden et al., 2014). **B.** Dynamical ellipticity. Hydrostatic $\delta H/H_0$ with $H = H(\phi) = 6.094\,x\,10^5\,x\,\phi^2$, $\delta H = H(\phi) - H_0$ and present-day H_0 = 0.00324 (Berger and Loutre, 1994) (green line); mantle $\delta H/H_0$ with H_0 = 0.003274 (Ghelichkhan et al., 2021) is added to hydrostatic $\delta H/H_0$ (orange line). The solid blue circle and blue line indicate $\delta H/H_0$ measured at Site 964 at 3 Ma (Lourens et al., 2001) and Site 926 for 0-25 Ma (Pälike and Shackleton, 2000) added to hydrostatic $\delta H/H_0$. The purple closed circles are estimated $\delta H/H_0$ for Sites U1410 (42.5 Ma) and 1262 (55 Ma) obtained by identifying the ages of the La2004 p model values that match the measured values for the two sites (projecting to ~39 Ma and ~40 Ma, respectively; see horizontal and vertical thin lines) (see also **Fig. 6B**).